Physics of Fluids ARTICLE scitation.org/journal/phf

Construction of knotted vortex tubes with the writhe-dependent helicity

Cite as: Phys. Fluids 31, 047101 (2019); doi: 10.1063/1.5088015
Submitted: 7 January 2019 • Accepted: 8 March 2019 •
Published Online: 1 April 2019

Shiying Xiong[1] and Yue Yang[1,2,a)]

AFFILIATIONS

[1]State Key Laboratory for Turbulence and Complex Systems, College of Engineering, Peking University, Beijing 100871, China
[2]CAPT and BIC-ESAT, Peking University, Beijing 100871, China

Note: This paper is part of the special issue from the 10th National Congress on Fluid Mechanics of China
[a)]**Electronic mail:** yyg@pku.edu.cn.

ABSTRACT

We propose a feasible method for constructing knotted vortex tubes with the finite thickness and arbitrary complexity and develop an accurate algorithm to implement this method in numerical simulations. The central axis of the knotted vortex tube is determined by the parametric equation of a given smooth and non-degenerate closed curve. The helicity of the vortex tube is only proportional to the writhe of the vortex axis, a geometric measure for coiling of vortex tubes. This vortex construction can facilitate the investigation of the conversion of writhe to twist in the helicity evolution of knotted vortex tubes. As examples, we construct velocity–vorticity fields of trefoil, cinquefoil, and septafoil vortex knots. These vortex knots are used as initial conditions in the direct numerical simulation of viscous incompressible flows in a periodic box. In the evolution of vortex knots from simple flows to turbulent-like flows, all the knots are first untied. Then the vortex topology is invariant and the helicity is almost conserved for the trefoil knot, whereas the helicity decays rapidly during the breakdown and coaxial interactions of pinch-off vortex rings for cinquefoil and septafoil knots.

I. INTRODUCTION

Helicity is a topological measure of linking and knotting of vortex lines[1,2] and is an invariant of the Euler equation of ideal fluid flows. The importance of helicity is underscored by the growing impact of links and knots on various physical systems, e.g., fluids,[3] plasmas,[4] and liquid crystals,[5] and by the emerging experimental technique for the complete measurement of helicity.[6]

However, the analysis of helicity is very challenging for general flows. Similar to the analysis of magnetic helicity,[7] if a flow field can be divided into subregions bounded by vortex surfaces, the helicity can be decomposed into a sum of the internal helicity, produced by the vorticity and induced velocity inside each subregion, and the external helicity, produced by the induced velocity inside each subregion and the vorticity inside the other subregions. The external helicity can be comprehensively characterized by the linking number and vorticity flux.[8,9] On the other hand, the internal helicity is only known to be related to the geometry, topology, and vorticity distribution of vortex lines within a vortex surface, and it is difficult to be explicitly expressed and accurately quantified.

The issue of characterizing the internal helicity can be partially resolved for some special cases, so it is possible to calculate the helicity in some flow fields with finite-sized vortex tubes, instead of using the analysis based on vortex filaments.[2,4] For an unknotted vortex ring consisting of nested toroidal vortex surfaces, the helicity can be derived as an explicit expression based on toroidal and poloidal vorticity fluxes.[7,10] This expression is generalized to knotted vortex tubes by introducing a "zero-framed" coordinate system.[11]

In particular, Moffatt[12] noticed that the internal helicity of vortex tubes is related to the Călugăreanu invariant,[13] also referred to as the self-linking number.[14] The self-linking number is a sum of two geometric quantities, the writhe and the normalized total torsion. Thus coiling and twisting of vortex tubes are often considered as two factors affecting the helicity,[6,15–17] but it is difficult to isolate each of them in flow analysis. Although the experiment of helical vortex leapfrogging[6] shows some evidence that the mechanism of conversion of writhe to twist (and vice versa) during vortex reconnection is important for the helicity conservation even in a viscous flow, the computational investigation of the conversion between writhe

and twist in a complex, fully three-dimensional phenomenon is still extremely challenging.[18]

In the present study, we extend the method of Chui and Moffatt[11] for magnetic flux tubes to construct the vorticity fields for knotted vortex tubes. The central axis of the vortex tube is prescribed by a smooth and non-degenerate closed curve. Thus this method can construct a vortex tube with the arbitrary geometry and topology specified by the given parametric equation of curves, and it appears to be more feasible for constructing complex vortex knots than the methods[19,20] relying on tailored Clebsch potentials.[21] Furthermore, we prove that the generated vorticity field from the present method is strictly divergence-free, without using the additional projection which may slightly modify the specified vorticity of vortex tubes.[17,22] In particular, the helicity of our constructed vortex tubes only depends on the writhe without the normalized total torsion, so we can isolate the effect of the writhe in the investigation of helicity, e.g., the conversion between writhe and twist.

Then we develop an accurate numerical algorithm to construct the compactly supported vorticity of knotted vortex tubes in Cartesian coordinates. In principle, our method can generate knotted tubes with finite thicknesses and arbitrary complexities. As examples, we construct trefoil, cinquefoil, and septafoil vortex knots. The corresponding vorticity fields are used as initial conditions of the direct numerical simulation (DNS). The evolution of the vortex knots involves signature vortex dynamics, such as vortex knot untying,[16,23] reconnection,[24,25] and breakdown.[26]

The outline of this paper is as follows: In Sec. II, we develop a theoretical method to generate the vorticity field of a vortex tube from a given parametric curve. In Sec. III, we describe the numerical algorithm for the vorticity construction in Cartesian coordinates, and then construct three knotted vortex tubes with increasing complexity. In Sec. IV, we carry out the DNS of the vortex knots and discuss the vortex dynamics. Some conclusions are drawn in Sec. V.

II. THEORETICAL CONSTRUCTION OF VORTEX TUBES

A. Parametric curve

The initial vortex tube is constructed from a given continuous and differentiable closed curve C without vanishing curvature in three-dimensional Euclidean space $\mathbb{R}^3$. The parametric equation of C is $\boldsymbol{x} = \boldsymbol{c}(s)$, where $\boldsymbol{x} = (x, y, z)$ denotes spatial Cartesian coordinates and $s \in [0, L_C)$ is the arc-length parameter with the length of curve L_C. The Frenet–Serret frame on C is

$$\begin{cases} \dfrac{\mathrm{d}\boldsymbol{T}}{\mathrm{d}s} = \kappa \boldsymbol{N}, \\ \dfrac{\mathrm{d}\boldsymbol{N}}{\mathrm{d}s} = -\kappa \boldsymbol{T} + \tau \boldsymbol{B}, \\ \dfrac{\mathrm{d}\boldsymbol{B}}{\mathrm{d}s} = -\tau \boldsymbol{N}, \end{cases} \tag{1}$$

where $\boldsymbol{T} \equiv \mathrm{d}\boldsymbol{c}/\mathrm{d}s$ denotes the unit tangent, $\boldsymbol{N} \equiv (\mathrm{d}\boldsymbol{T}/\mathrm{d}s)/|\mathrm{d}\boldsymbol{T}/\mathrm{d}s|$ denotes the unit normal, $\boldsymbol{B} \equiv \boldsymbol{T} \times \boldsymbol{N}$ denotes the unit binormal, κ denotes the curvature, and τ denotes the torsion of the curve.

The local polar coordinate system[11] along curve C is introduced to facilitate the construction of the vorticity $\boldsymbol{\omega} \equiv \nabla \times \boldsymbol{u}$ of vortex tubes, where $\boldsymbol{u}$ denotes the velocity. Figure 1 illustrates the local polar coordinates (ρ, θ) in the plane S_C spanned by $\boldsymbol{N}$ and $\boldsymbol{B}$ and normal to $\boldsymbol{T}$, where $\rho = |\boldsymbol{x} - \boldsymbol{c}| \geq 0$ is the distance from $\boldsymbol{c}(s)$ and $\theta \in [0, 2\pi)$ is the angle from the direction of unit normal $\boldsymbol{N}$ in S_C. Thus Cartesian coordinates $\boldsymbol{x}$ can be expressed as

$$\boldsymbol{x} = \boldsymbol{c}(s) + \rho \cos\theta \boldsymbol{N} + \rho \sin\theta \boldsymbol{B}, \tag{2}$$

and curve C is considered as the central axis of the vortex tube.

Equation (2) gives the transformation between coordinate systems (s, ρ, θ) and (x, y, z). From Eqs. (1) and (2), we derive the Jacobian matrix

$$\boldsymbol{J} \equiv \begin{pmatrix} \dfrac{\partial x}{\partial s} & \dfrac{\partial x}{\partial \rho} & \dfrac{\partial x}{\partial \theta} \\ \dfrac{\partial y}{\partial s} & \dfrac{\partial y}{\partial \rho} & \dfrac{\partial y}{\partial \theta} \\ \dfrac{\partial z}{\partial s} & \dfrac{\partial z}{\partial \rho} & \dfrac{\partial z}{\partial \theta} \end{pmatrix} \tag{3}$$

between the two systems as

$$\begin{aligned} \boldsymbol{J} = [&(1 - \kappa\rho\cos\theta)\boldsymbol{T} - \tau\rho\sin\theta\boldsymbol{N} + \tau\rho\cos\theta\boldsymbol{B}; \cos\theta\boldsymbol{N} \\ &+ \sin\theta\boldsymbol{B}; -\rho\sin\theta\boldsymbol{N} + \rho\cos\theta\boldsymbol{B}], \end{aligned} \tag{4}$$

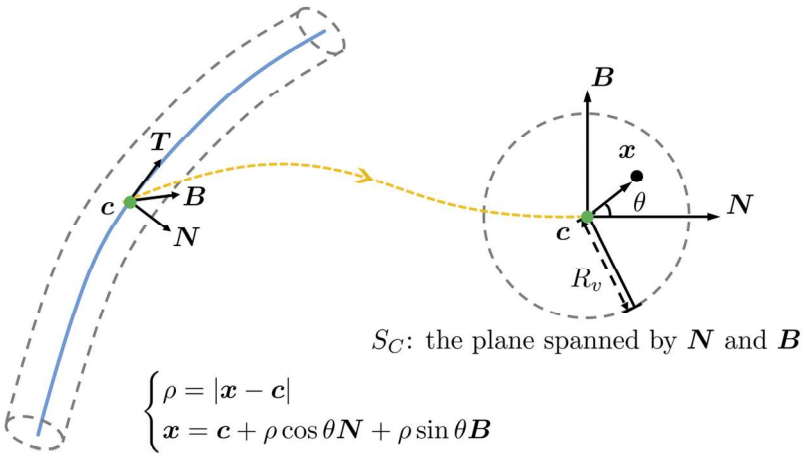

FIG. 1. The schematic diagram on the relation between coordinates (s, ρ, θ) and (x, y, z). The vortex tube is sketched by dashed curves, and its central axis is marked by the blue solid curve.

and the Jacobian determinant is

$$\det(\boldsymbol{J}) = \rho(1 - \rho\kappa\cos\theta). \tag{5}$$

In the subdomain $0 < \rho < R_\kappa$ with the minimum radius of curvature $R_\kappa \equiv \min(1/\kappa)$, the mapping from (s, ρ, θ) to (x, y, z) in Eq. (2) is locally invertible owing to $\det(\boldsymbol{J}) > 0$. In addition, if curve C is not self-intersecting, s can be uniquely determined by $\boldsymbol{x}$ at $\rho = 0$. Since the points in the proximity of C have small ρ, we assume that the radius of the vortex tube $R_v < R_\kappa$ is so small that (s, ρ) can be uniquely determined by $\boldsymbol{x}$ in the subdomain $\rho < R_v$.

B. Vorticity of the vortex tube

Based on the coordinate system (s, ρ, θ), we specify the vorticity of vortex tubes as

$$\boldsymbol{\omega}(s, \rho, \theta) = \Gamma f(\rho)\boldsymbol{T}(s), \tag{6}$$

where the constant Γ denotes the strength of the vorticity flux along vortex axis C, and the compactly supported kernel function $f(x)$ with $x \in [0, \infty)$ satisfies

$$\begin{cases} f(x) = 0, \ x \geq R_v, \\ \displaystyle\int_0^{R_v} f(x)x\,\mathrm{d}x = \frac{1}{2\pi}. \end{cases} \tag{7}$$

As proved below, the vector field constructed by Eq. (6) is solenoidal, which satisfies the definition of vorticity.

Theorem 1. *The vector field constructed by Eq. (6) is divergence-free.*

Proof 1. *Taking the divergence of Eq. (6), we have*

$$\begin{aligned} \nabla\cdot\boldsymbol{\omega}(s, \rho, \theta) &= \Gamma[\nabla f(\rho)\cdot\boldsymbol{T}(s) + f(\rho)\nabla\cdot\boldsymbol{T}(s)] \\ &= \Gamma\left[\frac{\mathrm{d}f(\rho)}{\mathrm{d}\rho}\nabla\rho\cdot\boldsymbol{T}(s) + f(\rho)\frac{\mathrm{d}\boldsymbol{T}}{\mathrm{d}s}\cdot\nabla s\right]. \end{aligned} \tag{8}$$

Applying the inverse function theorem to Eq. (4), we have

$$\nabla s = \frac{\boldsymbol{T}}{1 - \kappa\rho\cos\theta}, \quad \nabla\rho = \cos\theta\boldsymbol{N} + \sin\theta\boldsymbol{B}. \tag{9}$$

Substituting Eq. (9) into Eq. (8) yields $\nabla\cdot\boldsymbol{\omega} = 0$.

We remark that the vorticity Eq. (6) constructed in the local polar coordinates is uniquely defined in the Cartesian coordinates $\boldsymbol{x} \in \mathbb{R}^3$ because (s, ρ) and (x, y, z) have one-to-one mapping in the subdomain $\rho < R_v$ and Eq. (6) is independent of θ. Furthermore, Eq. (6) is vanishing in the subdomain $\rho \geq R_v$ where the mapping from (s, ρ, θ) to (x, y, z) can be singular.

C. Helicity of the vortex tube

In this subsection, we demonstrate that the specific vorticity Eq. (6) corresponds to the vortex tubes with the writhe-dependent helicity. Here, the helicity of a flow field is defined as

$$H \equiv \int_\Omega h\,\mathrm{d}\Omega, \tag{10}$$

where $h \equiv \boldsymbol{u}\cdot\boldsymbol{\omega}$ is the helicity density, Ω denotes the entire flow domain, and $\mathrm{d}\Omega$ is the volume element. The velocity $\boldsymbol{u}$ can be obtained from the vorticity via the Biot–Savart law, and then the helicity becomes

$$H = \frac{1}{4\pi}\int_\Omega\int_\Omega \frac{\boldsymbol{\omega}(\boldsymbol{x})\cdot\boldsymbol{\omega}(\boldsymbol{x}')\times(\boldsymbol{x} - \boldsymbol{x}')}{|\boldsymbol{x} - \boldsymbol{x}'|^3}\mathrm{d}\Omega\mathrm{d}\Omega', \tag{11}$$

where $\mathrm{d}\Omega'$ is the volume element at $\boldsymbol{x}'$.

In general, the helicity is hard to calculate by the multi-volume integral in Eq. (11), but it can be computable for some special velocity–vorticity fields. For the knotted vortex tubes consisting of nested toroidal vortex surfaces, Chui and Moffatt[11] proposed a feasible approach to obtain the explicit expression of helicity based on the "zero-framed" coordinate system

$$\begin{cases} \varsigma = s, \\ \chi = \phi_v(s, \rho, \theta), \\ \phi = \phi_a(s, \theta). \end{cases} \tag{12}$$

Here, $\phi_v(s, \rho, \theta)$ is a vortex-surface field (VSF)[27] surrounding vortex axis C. The VSF satisfies the constraint

$$\boldsymbol{\omega}\cdot\nabla\phi_v = 0, \tag{13}$$

i.e., the isosurface of ϕ_v is a vortex surface consisting of vortex lines. Moreover, $\phi_a(s, \theta)$ in Eq. (12) denotes a special angle variable which makes the ribbon-like isosurface of ϕ_a = constant "untwisted" in the sense that its boundaries C at $\chi = 0$ and Γ_ϕ at $\chi = 1$ have vanishing linking number.[11]

With the aid of the zero-framed coordinate system, toroidal and poloidal vorticity flux functions $T(x)$ and $P(x)$ in the helicity calculation for unknotted vortex rings[7,10] are extended to knotted vortex tubes.[11] Here, $T(x)$ denotes the vorticity flux through the cross section $S_\varsigma(x)$ at ς = constant with $(\chi, \phi) \in [0, x] \times [0, 2\pi)$ and $P(x)$ denotes the vorticity flux through the ribbon $R_\phi(x)$ at ϕ = constant with $(\varsigma, \chi) \in [0, L_C) \times [0, x]$.

In Eq. (12), the VSF $\chi = \phi_v(s, \rho, \theta)$ can be constructed from the vorticity[27] by solving the constraint Eq. (13). Since $\boldsymbol{\omega}$ in Eq. (6) is normal to $\nabla\rho$ in Eq. (9) as $\boldsymbol{\omega}\cdot\nabla\rho = 0$, we simply choose

$$\chi = \frac{\rho}{R_v} \tag{14}$$

as the normalized VSF. The angle variable $\phi = \phi_a(s, \theta)$ is set to be[11]

$$\phi = \theta + \frac{2\pi\mathcal{L}_S}{L_C}s, \tag{15}$$

where the self-linking number[14]

$$\mathcal{L}_S = W_r + T_t \tag{16}$$

is decomposed into the writhe

$$W_r = \frac{1}{4\pi}\oint_C\oint_C \frac{[\boldsymbol{N}(s)\times\boldsymbol{N}(s')]\cdot[\boldsymbol{c}(s) - \boldsymbol{c}(s')]}{|\boldsymbol{c}(s) - \boldsymbol{c}(s')|^3}\mathrm{d}s\mathrm{d}s' \tag{17}$$

and the normalized total torsion[12]

$$T_t = \frac{1}{2\pi}\oint_C \tau\mathrm{d}s. \tag{18}$$

The extra part $2\pi\mathcal{L}_S s/L_C$ in Eq. (15) offsets the twist generated on the ribbon defined by $\boldsymbol{c}$ and $\boldsymbol{N}$.[12]

After establishing the zero-framed coordinate system, Chui and Moffatt[11] derived a general expression of helicity as

$$H = 2\int_0^1 T(x)\frac{\mathrm{d}P(x)}{\mathrm{d}x}\mathrm{d}x. \tag{19}$$

We substitute Eqs. (14) and (15) into Eq. (12) and apply Eq. (2) to yield a specific transformation between coordinate systems (ς, χ, ϕ) and (x, y, z) as

$$\boldsymbol{x} = \boldsymbol{c}(\varsigma) + R_v\chi\left[\cos\left(\phi - \frac{2\pi\mathcal{L}_S}{L_C}\varsigma\right)\boldsymbol{N}(\varsigma) + \sin\left(\phi - \frac{2\pi\mathcal{L}_S}{L_C}\varsigma\right)\boldsymbol{B}(\varsigma)\right]. \tag{20}$$

Instead of using the implicit methods,[11,28] we compute the toroidal and poloidal vorticity fluxes in Eq. (19) directly from their definitions as

$$T(x) \equiv \iint_{S_\varsigma(x)} \boldsymbol{\omega}\cdot\boldsymbol{n}\,\mathrm{d}S = \int_0^x\int_0^{2\pi}\boldsymbol{\omega}\cdot\left(\frac{\partial\boldsymbol{x}}{\partial\chi}\times\frac{\partial\boldsymbol{x}}{\partial\phi}\right)\mathrm{d}\phi\mathrm{d}\chi \tag{21}$$

and

$$P(x) \equiv \iint_{R_\phi(x)} \boldsymbol{\omega}\cdot\boldsymbol{n}\,\mathrm{d}S = \int_0^x\oint_C\boldsymbol{\omega}\cdot\left(\frac{\partial\boldsymbol{x}}{\partial\varsigma}\times\frac{\partial\boldsymbol{x}}{\partial\chi}\right)\mathrm{d}\varsigma\,\mathrm{d}\chi, \tag{22}$$

respectively, where $\mathrm{d}S$ denotes the surface element and $\boldsymbol{n}$ denotes the normal of S_ς or R_ϕ. Substituting Eqs. (6) and (20) into Eqs. (21) and (22) yields

$$\begin{cases} T(x) = 2\pi\Gamma R_v^2\displaystyle\int_0^x \chi f(\chi R_v)\,\mathrm{d}\chi, \\ P(x) = 2\pi\Gamma R_v^2\left(\mathcal{L}_S - \dfrac{1}{2\pi}\displaystyle\oint_C\tau\mathrm{d}\varsigma\right)\int_0^x\chi f(\chi R_v)\,\mathrm{d}\chi. \end{cases} \tag{23}$$

Finally, substituting Eq. (23) with Eqs. (16) and (18) into Eq. (19), we obtain

$$H = \Gamma^2 W_r. \tag{24}$$

Therefore, the helicity of the vortex tube constructed by Eq. (6) is only proportional to the writhe without the contribution from the twisting of vortex lines inside the tube, which can isolate the writhe effect in the study of the internal helicity of vortex tubes.

III. NUMERICAL CONSTRUCTION OF KNOTTED VORTEX TUBES

A. Transformation of coordinate systems

The vorticity Eq. (6) is specified in terms of polar coordinates (s, ρ) along curve C, but in the numerical implementation, we construct $\boldsymbol{\omega}(\boldsymbol{x})$ in terms of Cartesian coordinates $\boldsymbol{x}$, so we need to transform $\boldsymbol{x}$ into (s, ρ) by Eq. (2). For a given $\boldsymbol{x}\in\mathbb{R}^3$, we determine (s, ρ) by

$$\begin{cases} s \in \underset{\zeta}{\operatorname{argmin}}|\boldsymbol{x} - \boldsymbol{c}(\zeta)|, \\ \rho = \underset{\zeta}{\min}\,|\boldsymbol{x} - \boldsymbol{c}(\zeta)|, \end{cases} \tag{25}$$

and the validity of Eq. (25) is justified below.

Theorem 2. *The coordinates (s, ρ) defined by Eq. (25) are identical to those implicitly determined by Eq. (2) in the subdomain with $\rho < R_v$.*

Proof 2. *For given $\boldsymbol{x}\in\mathbb{R}^3$, suppose (s, ρ) is determined by Eq. (25) in the subdomain with $\rho < R_v$. Then s must be a stationary point of $|\boldsymbol{x} - \boldsymbol{c}(\zeta)|^2$ from Fermat's theorem, i.e.,*

$$\left.\frac{\mathrm{d}|\boldsymbol{x} - \boldsymbol{c}(\zeta)|^2}{\mathrm{d}\zeta}\right|_{\zeta=s} = -2[\boldsymbol{x} - \boldsymbol{c}(s)]\cdot\boldsymbol{T}(s) = 0. \tag{26}$$

Hence, $\boldsymbol{x}$ corresponding to s is on the plane S_C normal to curve C, and $\boldsymbol{x}$ can be expressed by Eq. (2). Since the mapping between (s, ρ) and $\boldsymbol{x}$ is one-to-one in the subdomain with $\rho < R_v$, the coordinates (s, ρ) determined by Eq. (25) are the same as those implicitly determined by Eq. (2).

We develop a very accurate algorithm for computing Eqs. (6) and (25), which is described in Appendix A in detail. We find that various implementation methods for Eq. (25) can have an impact on the consistency of helicity calculations and the smoothness of the constructed vorticity field from numerical experiments, so the algorithm design is critical for the accurate vorticity construction.

B. Construction of knotted vortex tubes

We construct vortex tubes in the form of three given torus knots,[29] and their parametric equations $\boldsymbol{c}(\zeta) = (c_x(\zeta), c_y(\zeta), c_z(\zeta))$ are

$$\begin{cases} c_x(\zeta) = \pi + (R_t + r_t\cos(q\zeta))\cos(p\zeta)), \\ c_y(\zeta) = \pi + (R_t + r_t\cos(q\zeta))\sin(p\zeta)), \\ c_z(\zeta) = \pi - 1.5 - r_t\sin(q\zeta), \end{cases} \tag{27}$$

where $R_t = 1$ and $r_t = 0.5$ are the major and minor radii of a torus, respectively, and (p, q) are selected as (2, 3), (2, 5), and (2, 7), which represent trefoil knot with $\mathcal{L}_S = 6$, cinquefoil knot with $\mathcal{L}_S = 10$, and septafoil knot with $\mathcal{L}_S = 14$, respectively.[30] Here, $\zeta\in[0, 2\pi)$ is not an arc-length parameter, but this does not affect the vorticity construction because we can normalize the unit tangent by Eq. (B1) in Appendix B.

In the specified vorticity Eq. (6), the strength of vorticity flux is set to $\Gamma = 2$ and the vorticity flux distribution f is set to be a Gaussian function

$$f(x) = \frac{1}{2\pi\sigma^2}\exp\left(-\frac{x^2}{2\sigma^2}\right), \tag{28}$$

where the standard deviation is set to $\sigma = \sigma_0$ with $\sigma_0 = 1/\left(8\sqrt{2\pi}\right) \approx 0.05$. The corresponding radius of the vortex tube is estimated as $R_v \approx 5\sigma$. The vortex tube with the small R_v contains over 99.999% of the vorticity magnitude in Eq. (6), so we consider this vorticity field as compactly supported.

We construct the knotted vortex tubes in a period box of side $L = 2\pi$ and calculate the incompressible velocity field by

$$\boldsymbol{u} = \mathcal{F}^{-1}\left(\frac{i\boldsymbol{k}\times\widehat{\boldsymbol{\omega}}}{|\boldsymbol{k}|^2}\right), \tag{29}$$

where $\mathcal{F}^{-1}$ denotes the operator of inverse Fourier transform, $\boldsymbol{k}$ denotes the wavenumber in Fourier space, and $\widehat{\boldsymbol{\omega}} = \mathcal{F}(\boldsymbol{\omega})$ denotes the Fourier coefficient of $\boldsymbol{\omega}$ with the Fourier transform operator $\mathcal{F}$. The computational domain is discretized on uniform grid points N^3 with $N = 512$.

We assess the quality of the numerical construction of three knotted vortex tubes with the writhe-dependent helicity by using

TABLE I. Summary of parameters and geometrical/topological quantities in the numerical construction of three torus vortex knots.

(p, q)	R_κ	W_r	T_t	$\mathcal{L}_S$	H	ϵ_H
(2, 3)	0.72	3.52	2.48	6	14.07	6.3×10^{-7}
(2, 5)	0.6	6.87	3.13	10	27.47	1.0×10^{-6}
(2, 7)	0.56	10.54	3.46	14	42.17	4.6×10^{-7}

Eq. (24). The important geometrical and topological quantities in the construction of torus knots are summarized in Table I. The geometric quantities R_κ, W_r, and T_t of the curve are calculated using formulas in Appendix B. The resultant R_κ verifies the assumption $R_v < R_\kappa$. The self-linking number $\mathcal{L}_S$ is calculated by Eq. (16), and the results agree with the definitions of three torus knots.

The helicity H is calculated by Eq. (10) with the numerical integration of the product of computed velocity Eq. (29) and vorticity Eq. (A14) over the periodic box. The relative numerical error in Eq. (24) is defined as

$$\epsilon_H \equiv \frac{|H - \Gamma^2 W_r|}{|H|}, \tag{30}$$

and the negligible errors in Table I indicate that the numerical construction is very accurate. The validation of Eq. (24) also indicates that the normalized total torsion T_t in Table I, characterizing the twist of the unit normal $\boldsymbol{N}$ along the vortex axis $\boldsymbol{c}$, does not contribute to the helicity for the specified form of vorticity Eq. (6).

Figure 2 shows isosurfaces of $|\boldsymbol{\omega}|$ for three vortex knots. We observe that the vorticity field is smooth and compact, so the constructed vortex knots are suitable for initial conditions of DNS. Moreover, the isosurfaces are color-coded by the helicity density, and all the vortex tubes have $h > 0$, indicating that velocity and vorticity fields have the same chirality.

We remark that $|\boldsymbol{\omega}|$ for Eq. (6) is an exact VSF owing to

$$\boldsymbol{\omega} \cdot \nabla |\boldsymbol{\omega}| = \Gamma^2 f(\rho) \frac{\mathrm{d}f(\rho)}{\mathrm{d}\rho} \boldsymbol{T}(s) \cdot \nabla \rho = 0, \tag{31}$$

as the vortex lines integrated from points on isosurfaces of $|\boldsymbol{\omega}|$ are perfectly on the surfaces. Thus, $|\boldsymbol{\omega}|$ can be used as the initial condition for the evolution of VSF[31] in the Lagrangian-like study of vortex dynamics.

The momentum of a vortex ring or knot in fluid at rest at infinity is related to the impulse[32]

$$\boldsymbol{I} \equiv \frac{1}{2} \iiint_{\mathbb{R}^3} \boldsymbol{x} \times \boldsymbol{\omega}(\boldsymbol{x}) \mathrm{d}\Omega \approx \frac{1}{2} \iiint_{\Omega} \boldsymbol{x} \times \boldsymbol{\omega}(\boldsymbol{x}) \mathrm{d}\Omega, \tag{32}$$

which can be approximated by the integral over the periodic domain Ω for the highly compact vortex tubes in Eq. (6) at the initial time. As a theoretical estimation for the vortex filament with vanishing thickness, substituting $\boldsymbol{\omega} \mathrm{d}\Omega = \Gamma \mathrm{d}\boldsymbol{c}$ implied by Eq. (6) to Eq. (32) yields

$$\boldsymbol{I} = \Gamma \boldsymbol{S}, \tag{33}$$

where $\boldsymbol{S} = \oint_C \boldsymbol{c} \times \mathrm{d}\boldsymbol{c}/2$ is the directed area enclosed by curve C.[33] From Eq. (33), the torus vortex knots specified by Eq. (27) have the same $\boldsymbol{I} = (0, 0, 4.5\pi)$ for $(p, q) = (2, 3)$, $(2, 5)$, and $(2, 7)$. For the constructed knotted vortex tubes with finite thicknesses, the numerical integration of Eq. (32) also gives $\boldsymbol{I} \approx (0, 0, 14.17)$, very close to the result from Eq. (33), for all three vortex knots at the initial time. Since the impulse is a motion invariant,[32] it helps to characterize the evolutionary geometry of vortex knots, which will be discussed in Sec. IV B.

IV. EVOLUTION OF KNOTTED VORTEX TUBES

A. DNS

We take velocity fields of trefoil, cinquefoil, and septafoil vortex knots as initial conditions and calculate the evolution of each vortex knot using DNS. The fluid velocity field $\boldsymbol{u}(\boldsymbol{x}, t)$ of an incompressible viscous flow is governed by Navier–Stokes equations

$$\begin{cases} \dfrac{\partial \boldsymbol{u}}{\partial t} + (\boldsymbol{u} \cdot \nabla)\boldsymbol{u} = -\dfrac{1}{\rho}\nabla p + \nu \nabla^2 \boldsymbol{u}, \\ \nabla \cdot \boldsymbol{u} = 0, \end{cases} \tag{34}$$

where t denotes the time, p denotes the pressure, ρ denotes the density, and ν denotes the kinematic viscosity.

The DNS is performed to solve Eq. (34) in the periodic box using a standard pseudo-spectral method.[34] Aliasing errors are removed using the two-third truncation method with the maximum wavenumber $k_{\max} \approx N/3$. The Fourier coefficient $\widehat{\boldsymbol{u}} = \mathcal{F}(\boldsymbol{u})$ of the velocity is advanced in time using a second-order Adams–Bashforth method, and the time step is chosen to ensure the Courant–Friedrichs–Lewy number less than 0.5 for numerical stability and accuracy. The numerical solver used in this DNS has been validated and used in various applications.[35,36]

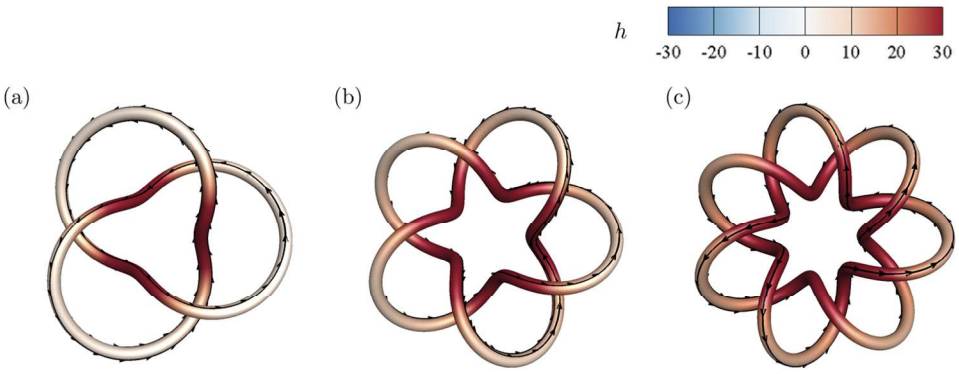

FIG. 2. Isosurfaces of $|\boldsymbol{\omega}| = 40$ of initial knotted vortex tubes. The isosurfaces are color-coded by the helicity density. Some vortex lines are integrated on the surfaces. (a) Trefoil knot, (b) cinquefoil knot, and (c) septafoil knot.

In the present DNS, we take $\nu = 0.001$, and the Reynolds number is $Re \equiv \Gamma/\nu = 2000$, which is comparable to the choices of Γ in previous simulations of vortex tubes.[17,37,38] The spatial resolution $k_{\max}\eta$ is always greater than 2.7 in the temporal evolution from initial simple flows to turbulent-like flows at the late stage, which satisfies the criterion[39] $k_{\max}\eta > 1.5$ for resolving the smallest scales in turbulence. Here, $\eta = (\nu^3/\varepsilon)^{1/4}$ denotes the Kolmogorov scale with the mean dissipation rate $\varepsilon = \nu \sum_{\boldsymbol{k}} (|\boldsymbol{k}||\widehat{\boldsymbol{u}}|)^2$.

B. Numerical results

We present the major flow statistics and important events of topological changes of vortex tubes and then analyze the relations between the flow statistics and vortex dynamics. Figure 3 plots the temporal evolution of the total energy $E_{tot} = \sum_{\boldsymbol{k}} |\widehat{\boldsymbol{u}}|^2/2$, mean dissipation rate, and helicity. We observe that E_{tot} monotonically decays in all three cases, and ε generally decays but has an intermediate peak for the trefoil knot and two peaks for cinquefoil and septafoil knots. The occurrence of these intermediate peaks of ε can be related to the knot untying[16,23] and reconnection[24,40] of vortex tubes. By contrast, the helicity is associated with the linking number, writhe, and twist, and the conservation of H in viscous flows is generally unclear. Despite under the viscous effect, H for the trefoil knot is remarkably conserved, which agrees with the former observation in experiments[16] because as vortex knots disentangle, they can create helix-like coils with the same total helicity at the mean time. On the other hand, H for cinquefoil and septafoil knots decays sharply after a short transition time. These observations imply that, compared with the trefoil knot, some different vortex dynamics should play an important role in the evolution of cinquefoil and septafoil knots.

Figure 4 depicts the evolution of isosurfaces of $|\boldsymbol{\omega}|$ at $t = 1$, 2, 3, and 5. All the isosurfaces are color-coded by h. In general, the occurrence of important events of topological changes in the evolution of vortex knots coincides with the intermediate peaks of ε, and estimated occurrence times are summarized in Table II. All the vortex knots first untie into upper and bottom vortex rings with significant vortex reconnection. The untying time decreases with the increasing self-linking number of initial knots. The topological change of vortex lines/tubes causes the significant variation of h and the generation of notable negative h.

Subsequently, the topology of the two coiled rings untied from the trefoil knot does not change in time, and positive h on the rings is well preserved. By contrast, the bottom vortex rings untied from cinquefoil and septafoil knots "break down" into five and seven smaller vortex rings, respectively. This complicated topological change does not occur for the trefoil knot, and it appears to significantly weaken positive h or generate negative h so that H for cinquefoil and septafoil knots drop sharply around $t = 2$ and $t = 5$, respectively.

Additionally, a clear intermediate and highly distorted vortex ring is pinched off in the disentanglement of the initial septafoil knot, and then this intermediate ring accelerates towards the upper ring with coaxial interactions of vortex rings[41] and further breakdown. Thus the septafoil vortex knot evolves into a turbulent-like flow at the late stage, with a part of the energy spectrum close to Kolmogorov's five-third scaling (not shown).

In the evolution of vortex knots, the impulse $\boldsymbol{I}$ calculated from the numerical integration over Ω in Eq. (32) is invariant until the knots collide with themselves at the periodic boundary at late times (not shown). The finite energy dissipation rate in Fig. 3(b) implies that the circulation Γ of knotted vortex tubes generally decays with time, so the conservation of $\boldsymbol{I} \approx \Gamma \boldsymbol{S}$ from Eq. (33) suggests that the directed area $\boldsymbol{S}$ enclosed by the knots grows with time. Thus with increasing the knot complexity [q in Eq. (27)] and the corresponding increasing ε in Fig. 3(b), the expansion of vortex knots becomes faster, which is consistent with the observation in Fig. 4.

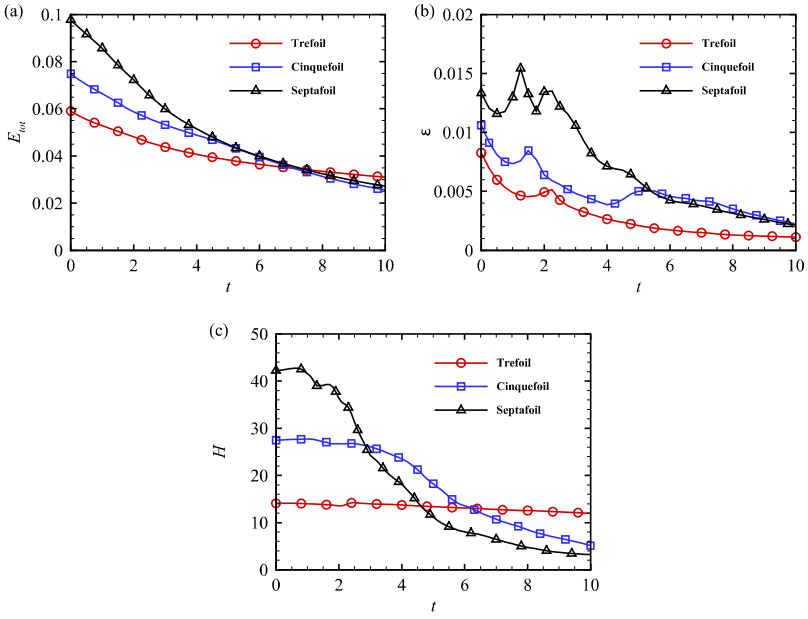

FIG. 3. Temporal evolution of (a) the total energy, (b) mean dissipation rate, and (c) helicity in the DNS of three vortex knots.

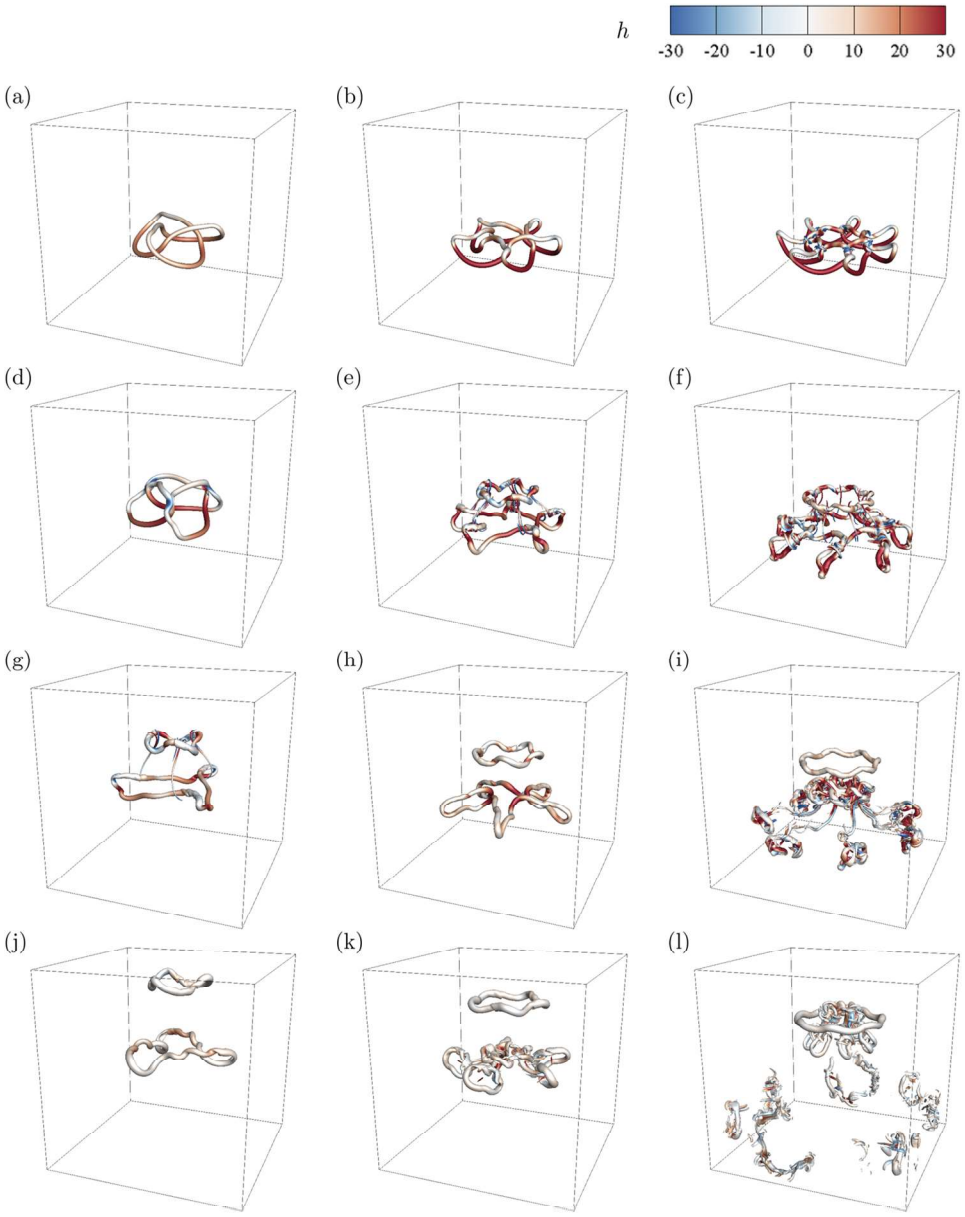

FIG. 4. Isosurfaces of $|\omega|$ in the temporal evolution of trefoil, cinquefoil, and septafoil knots (from left to right columns) at t = 1, 2, 3, and 5 (from upper to bottom rows). All the isosurfaces are color-coded by the helicity density. The isocontour values of $|\omega|$ are 35, 30, 25, and 17 at t = 1, 2, 3, and 5, respectively.

TABLE II. Estimated occurrence times of the events of topological changes in the evolution of vortex knots. The symbol ". . ." denotes the un-occurred event.

Event of topological change	Trefoil knot	Cinquefoil knot	Septafoil knot
Untying the knot	2.2	1.5	1.1
Breakdown of the bottom ring	. . .	4.9	2.1
Pinch off of the intermediate ring	. . .	. . .	2.5

V. CONCLUSIONS

We develop a feasible method for constructing knotted vortex tubes with the writhe-dependent helicity and arbitrary complexity. From the parametric equation of a given smooth and non-degenerate closed curve, we construct a vector field based on a local polar coordinate system along the curve. The vector magnitude, determined by a given kernel function, decays with the distance from the curve, and the vector direction is the same as the unit tangent of the nearest point on the curve. We prove that this vector field is strictly divergence-free, so it can be used as the initial

vorticity field of the vortex tube whose central axis is prescribed by the curve.

Within the framework of Chui and Moffatt,[11] we derive the explicit expression of the helicity of the constructed velocity–vorticity field and find that this helicity is only proportional to writhe of the curve, so we can isolate the effect of writhe in the investigation of helicity.

Corresponding to the theoretical construction, we propose an accurate and robust numerical algorithm for constructing knotted vortex tubes in Cartesian coordinates. The relative numerical errors in the helicity calculation of three typical torus vortex knots, including trefoil, cinquefoil, and septafoil knots, are negligible (less than 10^{-6}) on 512^3 uniform grid points in a periodic box.

We use the constructed velocity–vorticity fields as initial conditions of DNS and calculate the evolution three vortex knots in viscous incompressible flows. We find that all the initial knots are untied after a short time. Then the helicity is almost conserved in the evolution of the trefoil knot, which agrees with the former finding in experiments.[16] On the other hand, the decay of helicity in the evolution of cinquefoil and septafoil knots is remarkable. This appears to be related to complex topological changes of vortical structures, such as the breakdown and coaxial interactions of pinch-off vortex rings, other than the disentanglement of vortex knots.

Based on the proposed method for the numerical construction of vortex knots, we expect to carry out the large-scale DNS[42] and detailed, quantitative study[43,44] of highly complex vortex knots in future work, which can be useful to elucidate the conversion mechanism between writhe and twist in the evolution of helicity. Moreover, this work can be naturally extended to the study of magnetic flux tubes.

ACKNOWLEDGMENTS

The authors thank W. D. Su for helpful discussions. Numerical simulations were carried out on the TH-2A supercomputer in Guangzhou, China. This work was supported in part by the National Natural Science Foundation of China (Grant Nos. 11522215, 91541204, and 91841302).

APPENDIX A: NUMERICAL ALGORITHM FOR COMPUTING $\omega(x)$

First, we describe the idea of the algorithm for computing Eqs. (6) and (25). For a given $\boldsymbol{x}$ and a parametric curve C: $\boldsymbol{c}(\zeta)$, where ζ is not necessary to be an arc-length parameter, we seek a set for all the stationary points of $|\boldsymbol{x}-\boldsymbol{c}(\zeta)|$ as

$$S_\zeta(\boldsymbol{x}) = \{\zeta | (\boldsymbol{x}-\boldsymbol{c}(\zeta))\cdot \boldsymbol{T}(\zeta) = 0\}. \tag{A1}$$

For each $\zeta \in S_\zeta$, the corresponding pole distance in the plane S_C normal to curve C is

$$\rho_\zeta = |\boldsymbol{x}-\boldsymbol{c}(\zeta)|. \tag{A2}$$

Then Eq. (6) is calculated as

$$\boldsymbol{\omega}(\boldsymbol{x}) = \Gamma \sum_{\zeta\in S_\zeta(\boldsymbol{x})} f(\rho_\zeta)\boldsymbol{T}(\zeta). \tag{A3}$$

Note one $\boldsymbol{x}$ may correspond to multiple ζ in $S_\zeta(\boldsymbol{x})$, but only one ζ with $\rho_\zeta < R_v$ contributes to the summation in Eq. (A3) via the nontrivial kernel function $f(\rho_\zeta)$ defined in Eq. (7). Figure 5 illustrates

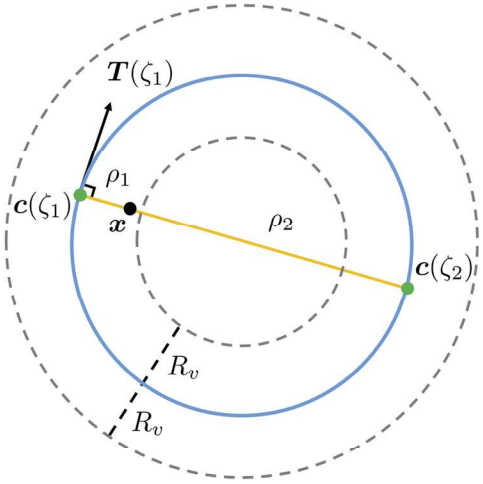

FIG. 5. The diagram for searching stationary points of $|\boldsymbol{x}-\boldsymbol{c}(\zeta)|$ and calculating $\boldsymbol{\omega}(\boldsymbol{x})$.

a simplified case of a vortex ring, for example. Here the given $\boldsymbol{x}$ corresponds to two stationary points ζ_1 and ζ_2 of $|\boldsymbol{x}-\boldsymbol{c}(\zeta)|$, and ζ_2 corresponds to $f(\rho_2) = 0$ with $\rho_2 > R_v$. Then Eq. (A3) becomes $\boldsymbol{\omega}(\boldsymbol{x}) = \Gamma f(\rho_1)\boldsymbol{T}(\zeta_1)$. We remark that if R_v in Eq. (6) is set to be too large, e.g., $R_v > R_\kappa$, the constructed vortex tube may self-intersect, which corresponds to multiple non-zero terms in Eq. (A3), and we can still compute a smooth vorticity field by Eq. (A3). However, Eq. (24) for calculating the helicity may not be accurate, which will be discussed in Appendix C.

Next we provide numerical details for calculating Eq. (A3) with the discretization of C. As sketched in Fig. 6, for a given, closed parametric curve C: $\boldsymbol{c}(\zeta)$ with $\zeta \in [0, L_\zeta)$, we divide C into N_C segments by N_C dividing points

$$\boldsymbol{c}_i = \boldsymbol{c}(\zeta_i),\ i = 1, 2, \ldots, N_C, \tag{A4}$$

with $\zeta_i = (i-1)\Delta\zeta$ and $\Delta\zeta = L_\zeta/N_C$. If N_C is sufficiently large, curve C can be approximated as a fold line connecting all the dividing points. Then the unit tangent on the line segment

$$l_i = \{\boldsymbol{c}_i + \lambda(\boldsymbol{c}_{i+1}-\boldsymbol{c}_i)\,|\,\lambda \in [0,1]\},\ i = 1, 2, \ldots, N_C, \tag{A5}$$

can be expressed as

$$\boldsymbol{T}_i = \frac{\boldsymbol{c}_{i+1}-\boldsymbol{c}_i}{|\boldsymbol{c}_{i+1}-\boldsymbol{c}_i|},\ i = 1, 2, \ldots, N_C, \tag{A6}$$

where subscripts $N_C + 1$ and 1 are equivalent. Then at each dividing point, we construct normal planes

$$S_i = \{\boldsymbol{x} | (\boldsymbol{x}-\boldsymbol{c}_i)\cdot \boldsymbol{T}_i = 0\},\ i = 1, 2, \ldots, N_C \tag{A7}$$

to divide the space in the proximity of curve C into N_C subdomains

$$\Omega_i = \{\boldsymbol{x} | (\boldsymbol{x}-\boldsymbol{c}_i)\cdot \boldsymbol{T}_i \geq 0 \text{ and } (\boldsymbol{x}-\boldsymbol{c}_{i+1})\cdot \boldsymbol{T}_{i+1} < 0\}. \tag{A8}$$

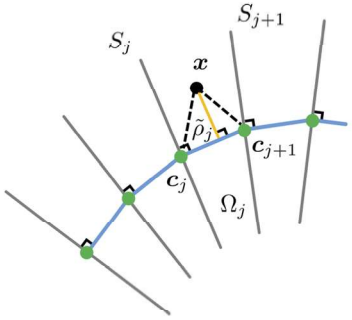

$$\boldsymbol{c}_j = \boldsymbol{c}(\zeta_j)$$

$$\boldsymbol{T}_j = (\boldsymbol{c}_{j+1} - \boldsymbol{c}_j)/|\boldsymbol{c}_{j+1} - \boldsymbol{c}_j|$$

$$\tilde{\zeta}_j = \frac{\zeta_{j+1}(\boldsymbol{x} - \boldsymbol{c}_j)\cdot\boldsymbol{T}_j + \zeta_j(\boldsymbol{c}_{j+1} - \boldsymbol{x})\cdot\boldsymbol{T}_j}{|\boldsymbol{c}_{j+1} - \boldsymbol{c}_j|}$$

$$\tilde{\rho}_j = \sqrt{|\boldsymbol{x} - \boldsymbol{c}_j|^2 - [(\boldsymbol{x} - \boldsymbol{c}_j)\cdot\boldsymbol{T}_j]^2}$$

FIG. 6. The diagram for discretization of curve C and determination of the curve parameter and the minimum distance between given $\boldsymbol{x}$ and C.

For a given $\boldsymbol{x}$, we first use Eq. (A8) to determine the subdomains $\boldsymbol{\Omega}_i$ containing $\boldsymbol{x}$. The subscripts of all the $\boldsymbol{\Omega}_i$ containing $\boldsymbol{x}$ are denoted by a set

$$\tilde{I}_\zeta(\boldsymbol{x}) = \{j|\boldsymbol{x} \in \boldsymbol{\Omega}_j\}. \tag{A9}$$

For each $j \in \tilde{I}_\zeta(\boldsymbol{x})$, ζ in $\boldsymbol{T}(\zeta)$ can be approximated as

$$\tilde{\zeta}_j = \frac{\zeta_{j+1}(\boldsymbol{x} - \boldsymbol{c}_j)\cdot\boldsymbol{T}_j + \zeta_j(\boldsymbol{c}_{j+1} - \boldsymbol{x})\cdot\boldsymbol{T}_j}{|\boldsymbol{c}_{j+1} - \boldsymbol{c}_j|}, \tag{A10}$$

so the discretized point set of ζ for Eq. (A1) is collected by

$$S_\zeta(\boldsymbol{x}) = \{\tilde{\zeta}_j|j \in \tilde{I}_\zeta(\boldsymbol{x})\}. \tag{A11}$$

For each $\tilde{\zeta}_j$, the distance $|\boldsymbol{x} - \boldsymbol{c}(\tilde{\zeta}_j)|$ is calculated by

$$\tilde{\rho}_j = \sqrt{|\boldsymbol{x} - \boldsymbol{c}_j|^2 - [(\boldsymbol{x} - \boldsymbol{c}_j)\cdot\boldsymbol{T}_j]^2}. \tag{A12}$$

Then the unit tangent in Eq. (A3) at $\tilde{\zeta}_j$ is approximated by the second-order central difference scheme as

$$\widetilde{\boldsymbol{T}}_j = \frac{\boldsymbol{c}(\tilde{\zeta}_j + \Delta\zeta) - \boldsymbol{c}(\tilde{\zeta}_j - \Delta\zeta)}{|\boldsymbol{c}(\tilde{\zeta}_j + \Delta\zeta) - \boldsymbol{c}(\tilde{\zeta}_j - \Delta\zeta)|}. \tag{A13}$$

Finally, we approximate Eq. (A3) for the vorticity Eq. (6) as

$$\boldsymbol{\omega}(\boldsymbol{x}) = \Gamma \sum_{j\in\tilde{I}_\zeta(\boldsymbol{x})} f(\tilde{\rho}_j)\widetilde{\boldsymbol{T}}_j. \tag{A14}$$

The procedure for the numerical construction of $\boldsymbol{\omega}(\boldsymbol{x})$ is summarized in Algorithm 1. This algorithm is more accurate and efficient than the simple traversal of all the dividing points of curve C for seeking minimum $|\boldsymbol{x} - \boldsymbol{c}_i|$ through numerical experiments.

ALGORITHM 1. Calculation of $\boldsymbol{\omega}(\boldsymbol{x})$.

Input: $\boldsymbol{x}$, $\boldsymbol{c}(\zeta)$, $f(\rho)$, Γ, and N_C
Output: $\boldsymbol{\omega}(\boldsymbol{x})$
Divide the space in the proximity of curve $\boldsymbol{c}(\zeta)$ into N_C subdomains by Eq. (A8)
Obtain $\tilde{I}_\zeta$ by Eq. (A9) at $\boldsymbol{x}$
Calculate $\tilde{\zeta}_j$ by Eq. (A10) and $\tilde{\rho}_j$ by Eq. (A12) for each $j \in \tilde{I}_\zeta$
Calculate $\widetilde{\boldsymbol{T}}_j$ by Eq. (A13) for given $\boldsymbol{c}(\zeta)$ at $\zeta = \tilde{\zeta}_j$
Calculate $\boldsymbol{\omega}(\boldsymbol{x})$ by (A14) with computed $\widetilde{\boldsymbol{T}}_j$ and given Γ and $f(\tilde{\rho}_j)$
Return $\boldsymbol{\omega}(\boldsymbol{x})$.

APPENDIX B: DIFFERENTIAL GEOMETRY OF A CLOSED PARAMETRIC CURVE

In Sec. III B, we introduce a continuous, differentiable, and non-degenerate closed curve C in three-dimensional Euclidean space $\mathbb{R}^3$ with the parametric equation $\boldsymbol{x} = \boldsymbol{c}(\zeta)$, where ζ is not necessary to be an arc-length parameter. The formulas for calculating geometric properties of C from $\boldsymbol{c}(\zeta)$ are listed below.

The Frenet–Serret frame can be expressed as

$$\begin{cases} \boldsymbol{T}(\zeta) = \dfrac{\boldsymbol{c}'(\zeta)}{|\boldsymbol{c}'(\zeta)|}, \\ \boldsymbol{N}(\zeta) = \dfrac{|\boldsymbol{c}'(\zeta)|}{|\boldsymbol{c}'(\zeta)\times\boldsymbol{c}''(\zeta)|}\boldsymbol{c}''(\zeta) - \dfrac{\boldsymbol{c}'(\zeta)\cdot\boldsymbol{c}''(\zeta)}{|\boldsymbol{c}'(\zeta)||\boldsymbol{c}'(\zeta)\times\boldsymbol{c}''(\zeta)|}\boldsymbol{c}'(\zeta), \\ \boldsymbol{B}(\zeta) = \dfrac{\boldsymbol{c}'(\zeta)\times\boldsymbol{c}''(\zeta)}{|\boldsymbol{c}'(\zeta)\times\boldsymbol{c}''(\zeta)|}, \end{cases} \tag{B1}$$

with

$$\boldsymbol{c}'(\zeta) = \frac{\mathrm{d}\boldsymbol{c}(\zeta)}{\mathrm{d}\zeta} \quad \text{and} \quad \boldsymbol{c}''(\zeta) = \frac{\mathrm{d}^2\boldsymbol{c}(\zeta)}{\mathrm{d}\zeta^2}. \tag{B2}$$

The curvature and torsion along the curve are

$$\begin{cases} \kappa(\zeta) = \dfrac{|\boldsymbol{c}'(\zeta)\times\boldsymbol{c}''(\zeta)|}{|\boldsymbol{c}'(\zeta)|^3}, \\ \tau(\zeta) = \dfrac{[\boldsymbol{c}'(\zeta)\times\boldsymbol{c}''(\zeta)]\cdot\boldsymbol{c}'''(\zeta)}{|\boldsymbol{c}'(\zeta)\times\boldsymbol{c}''(\zeta)|^2}, \end{cases} \tag{B3}$$

with

$$\boldsymbol{c}'''(\zeta) = \frac{\mathrm{d}^3\boldsymbol{c}(\zeta)}{\mathrm{d}\zeta^3}. \tag{B4}$$

The writhe and the normalized total torsion are calculated by

$$\begin{cases} W_r = \dfrac{1}{4\pi}\oint_C\oint_C \dfrac{[\boldsymbol{c}'(\zeta)\times\boldsymbol{c}'(\xi)]\cdot[\boldsymbol{c}(\zeta) - \boldsymbol{c}(\xi)]}{|\boldsymbol{c}(\zeta) - \boldsymbol{c}(\xi)|^3}\mathrm{d}\zeta\mathrm{d}\xi, \\ T_t = \dfrac{1}{2\pi}\oint_C \tau(\zeta)|\boldsymbol{c}'(\zeta)|\mathrm{d}\zeta. \end{cases} \tag{B5}$$

In the numerical implementation of these formulas, curve C is first divided into $N_C = 10^4$ segments in terms of ζ (see Appendix A). Then all the derivatives are calculated by the second-order central difference scheme, and the integrals are calculated by the numerical integration with the rectangle rule.

APPENDIX C: SELF-INTERSECTION OF THE KNOTTED VORTEX TUBE

As mentioned in Appendix A, the self-intersection of the vortex tube with finite thickness results in the inaccurate relationship

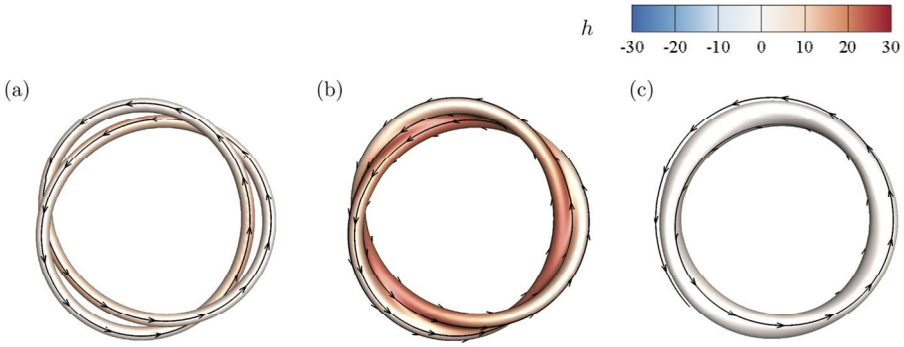

FIG. 7. Isosurfaces of $|\omega|$ of initial knotted vortex tubes. The isosurfaces are color-coded by the helicity density. Some vortex lines are integrated on the surfaces. (a) $\sigma = 0.5\sigma_0 \approx 0.025$, $|\omega| = 20$; (b) $\sigma = 1.5\sigma_0 \approx 0.075$, $|\omega| = 40$; and (c) $\sigma = 3\sigma_0 \approx 0.15$, $|\omega| = 18$.

in Eq. (24) between the helicity and the writhe of the vortex axis. We illustrate this breakdown using a series of trefoil vortex knots for which the vortex axis is determined by Eq. (27) with $(p, q) = (2, 3)$ and $(R_t, r_t) = (1, 0.1)$, and the thickness, i.e., the radius $R_v \approx 5\sigma$, is varied as $\sigma \in [0.5\sigma_0, 40\sigma_0]$ in the vorticity flux distribution Eq. (28).

Figure 7 depicts the isosurfaces of $|\omega|$ for the trefoil knots with a relatively large aspect ratio $R_t/r_t = 10$ and three different σ. As the thickness increases, the knotted tube becomes gradually self-crossing, and finally merges into an unknotted vortex ring. Although the tubes with varied σ have the identical vortex axis, the topology of the vortex lines therein and the distribution of the helicity density are very different.

Figure 8 compares the helicities calculated by Eqs. (10) and (24) for the knotted vortex tubes with a range of thicknesses. As σ increases, H from Eq. (24) with the same W_r and Γ is invariant, whereas H from Eq. (10) decays as illustrated in Fig. 7. In the extreme case in Fig. 7, the discrepancy on H becomes significant for $\sigma > \sigma_0$. By contrast, for the three knots constructed in Sec. III B and shown in Fig. 2, Eq. (24) is still accurate enough for $\sigma < 3\sigma_0$. Therefore, the present numerical algorithm can construct the smooth and self-intersecting knotted vortex tubes, but their helicity cannot be analyzed by Eq. (24).

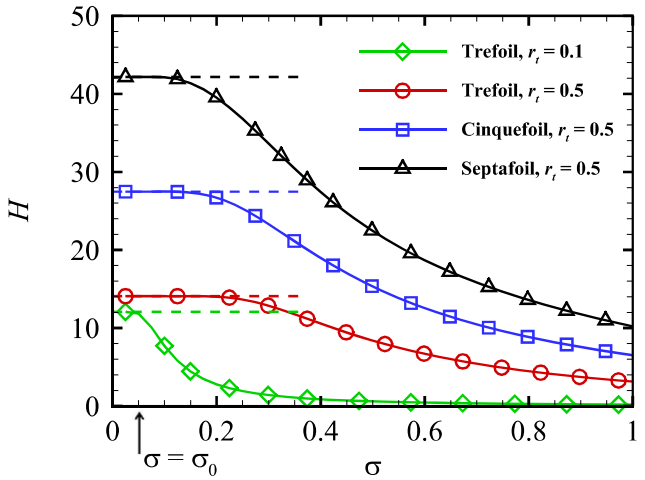

FIG. 8. The helicity of initial knotted vortex tubes with various thicknesses. Solid lines: H calculated by Eq. (10); dashed lines: H calculated by Eq. (24).

REFERENCES

[1] J. J. Moreau, "Constantes d'un îlot tourbillonnaire en fluide parfait barotrope," C. R. Acad. Sci. Paris **252**, 2810–2812 (1961).
[2] H. K. Moffatt, "The degree of knottedness of tangled vortex lines," J. Fluid Mech. **35**, 117–129 (1969).
[3] D. Kleckner and W. T. M. Irvine, "Creation and dynamics of knotted vortices," Nat. Phys. **9**, 253–258 (2013).
[4] R. L. Ricca and H. K. Moffatt, "The helicity of a knotted vortex filament," in *Topological Aspects of the Dynamics of Fluids and Plasmas* (Springer, 1992), pp. 225–236.
[5] A. Martinez, M. Ravnik, B. Lucero, R. Visvanathan, S. Žumer, and I. I. Smalyukh, "Mutually tangled colloidal knots and induced defect loops in nematic fields," Nat. Mater. **13**, 258–263 (2014).
[6] M. W. Scheeler, W. M. van Rees, H. Kedia, D. Kleckner, and W. T. M. Irvine, "Complete measurement of helicity and its dynamics in vortex tube," Science **357**, 487–491 (2017).
[7] M. A. Berger and G. B. Field, "The topological properties of magnetic helicity," J. Fluid Mech. **147**, 133–148 (1984).
[8] W. D. Su, "Helicity analysis and differential geometry," Ph.D. thesis, Peking University, 1998.
[9] J. Cantarella, "A general mutual helicity formula," Proc. R. Soc. London, Ser. A **456**, 2771–2779 (2000).
[10] M. D. Kruskal and R. M. Kulsrud, "Equilibrium of a magnetically confined plasma in a toroid," Phys. Fluids **1**, 265–274 (1958).
[11] A. Y. K. Chui and H. K. Moffatt, "The energy and helicity of knotted magnetic flux tubes," Proc. R. Soc. London, Ser. A **451**, 609–629 (1995).
[12] H. K. Moffatt and R. L. Ricca, "Helicity and the Călugăreanu invariant," Proc. R. Soc. London, Ser. A **439**, 411–429 (1992).
[13] G. Călugăreanu, "L'intégral de Gauss et l'analyse des noeuds tridimensionnels," Rev. Math. Pures Appl. **4**, 5–20 (1959).
[14] W. F. Pohl, "The self-linking number of a closed space curve," J. Math. Mech. **17**, 975–985 (1968).
[15] M. A. Berger, "Introduction to magnetic helicity," Plasma Phys. Controlled Fusion **41**, B167 (1999).
[16] M. W. Scheeler, D. Kleckner, D. Proment, G. L. Kindlmann, and W. T. M. Irvine, "Helicity conservation by flow across scales in reconnecting vortex links and knots," Proc. Natl. Acad. Sci. U. S. A. **111**, 15350–15355 (2014).
[17] R. M. Kerr, "Topology of interacting coiled vortex rings," J. Fluid Mech. **854**, R2 (2018).
[18] H. K. Moffatt, "Helicity-invariant even in a viscous fluid," Science **357**, 448 (2017).
[19] H. Kedia, D. Foster, M. R. Dennis, and W. T. M. Irvine, "Weaving knotted vector fields with tunable helicity," Phys. Rev. Lett. **117**, 274501 (2016).
[20] A. Chern, F. Knöppel, U. Pinkall, P. Schröder, and S. Weißmann, "Schrödinger's smoke," ACM Trans. Graphics **35**, 77 (2016).
[21] A. Clebsch, "Ueber die Integration der hydrodynamischen Gleichungen," J. Reine Angew. Math. **56**, 1–10 (1859).

[22]R. M. Kerr, "Swirling, turbulent vortex rings formed from a chain reaction of reconnection events," Phys. Fluids **25**, 065101 (2013).
[23]D. Kleckner, L. H. Kauffman, and W. T. M. Irvine, "How superfluid vortex knots untie," Nat. Phys. **12**, 650–655 (2016).
[24]S. Kida and M. Takaoka, "Vortex reconnection," Annu. Rev. Fluid. Mech. **26**, 169–189 (1994).
[25]L. D. G. Beardsell and G. Dumas, "Investigation of the viscous reconnection phenomenon of two vortex tubes through spectral simulations," Phys. Fluids **28**, 095103 (2016).
[26]S. Leibovich, "The structure of vortex breakdown," Ann. Rev. Fluid Mech. **10**, 221–246 (1978).
[27]Y. Yang and D. I. Pullin, "On Lagrangian and vortex-surface fields for flows with Taylor–Green and Kida–Pelz initial conditions," J. Fluid Mech. **661**, 446–481 (2010).
[28]G. Bateman, *MHD Instabilities* (MIT Press, 1978).
[29]X. Liu and R. L. Ricca, "Knots cascade detected by a monotonically decreasing sequence of values," Sci. Rep. **6**, 24118 (2016).
[30]K. Murasugi, "On the braid index of alternating links," Trans. Am. Math. Soc. **326**, 237–260 (1991).
[31]Y. Yang and D. I. Pullin, "Evolution of vortex-surface fields in viscous Taylor–Green and Kida–Pelz flows," J. Fluid Mech. **685**, 146–164 (2011).
[32]G. K. Batchelor, *An Introduction to Fluid Dynamics* (Cambridge University Press, 1967; 1973).
[33]J. Z. Wu, H. Y. Ma, and M. D. Zhou, *Vortical Flows* (Springer, 2015).
[34]R. S. Rogallo, "Numerical experiments in homogeneous turbulence," Technical Report No. TM81315, NASA, 1981.
[35]Y. Yang, D. I. Pullin, and I. Bermejo-Moreno, "Multi-scale geometric analysis of Lagrangian structures in isotropic turbulence," J. Fluid Mech. **654**, 233–270 (2010).
[36]T. Zheng, J. You, and Y. Yang, "Principal curvatures and area ratio of propagating surfaces in isotropic turbulence," Phys. Rev. Fluids **2**, 103201 (2017).
[37]H. Guan, Z. Wei, E. R. Rasolkova, and C. Wu, "Numerical simulations of two coaxial vortex rings head-on collision," Adv. Appl. Math. Mech. **8**, 616–647 (2016).
[38]M. Cheng, J. Lou, and T. T. Lim, "Numerical simulation of head-on collision of two coaxial vortex rings," Fluid Dyn. Res. **50**, 065513 (2018).
[39]S. B. Pope, *Turbulent Flows*, 1st ed. (Cambridge University Press, 2000).
[40]F. Hussain and K. Duraisamy, "Mechanics of viscous vortex reconnection," Phys. Fluids **23**, 021701 (2011).
[41]K. Shariff and A. Leonard, "Vortex rings," Annu. Rev. Fluid. Mech. **24**, 235–279 (1992).
[42]W. M. van Rees, F. Hussain, and P. Koumoutsakos, "Vortex tube reconnection at $Re = 10^4$," Phys. Fluids **24**, 075105 (2012).
[43]H. K. Moffatt, "Helicity and singular structures in fluid dynamics," Proc. Natl. Acad. Sci. U. S. A. **111**, 3663–3670 (2014).
[44]C. E. Laing, R. L. Ricca, and D. W. L. Sumners, "Conservation of writhe helicity under anti-parallel reconnection," Sci. Rep. **5**, 9224 (2015).